HHS Public Access

Author manuscript

Nat Struct Mol Biol. Author manuscript; available in PMC 2019 January 16.

Published in final edited form as:

Nat Struct Mol Biol. 2018 August ; 25(8): 660–668. doi:10.1038/s41594-018-0089-6.

Structural basis for the regulation of inositol trisphosphate receptors by Ca^{2+} and IP_3

Navid Paknejad[1,2] and **Richard K Hite**[1,*]

[1]Structural Biology Program, Memorial Sloan Kettering Cancer Center, New York, New York, USA

[2]Physiology, Biophysics and Systems Biology Graduate Program, Weill Cornell Medical College, New York, New York, USA

Abstract

Inositol trisphosphate receptors (IP_3R) are ubiquitous Ca^{2+}-permeable channels that mediate release of Ca^{2+} from the endoplasmic reticulum to regulate numerous processes including cell division, cell death, differentiation and fertilization. IP_3R is activated by both IP_3 and its permeant ion Ca^{2+}. At high concentrations, however, Ca^{2+} inhibits activity ensuring precise spatiotemporal control over intracellular Ca^{2+}. Despite extensive characterization of IP_3R, the mechanisms by which these molecules control channel gating have remained elusive. Here, we present structures of full-length human type 3 IP_3R in ligand-bound and ligand-free states. Multiple IP_3-bound structures demonstrate that the large cytoplasmic domain provides a platform for propagation of long-range conformational changes to the ion conduction gate. Structures in the presence of Ca^{2+} reveal two Ca^{2+} binding sites that induce the disruption of numerous interactions between subunits, thereby inhibiting IP_3R. These structures thus begin to provide a mechanistic basis for understanding the regulation of IP_3R.

Correspondence to hiter@mskcc.org.

Accession Codes

Cryo-EM maps have been deposited in the EMDB under accession codes EMD-7978 for the full channel apo map, EMD-7979 for the apo CD focus refinement map, EMD-7980 for the apo S1–S4 focus refinement map, EMD-7981 for the IP_3 class 1 map, EMD-7982 for the IP_3 class 1 CD focus refinement map, EMD-7984 for the IP_3 class 2 map, EMD-7982 for the IP_3 class 2 CD focus refinement map, EMD-7985 for the IP_3 class 3 map, EMD-7986 for the IP_3 class 4 map, EMD-7987 for the IP_3 class 5 map, EMD-7888 for the full channel Ca^{2+}-bound map, EMD-7990 for the Ca^{2+}-bound TMD focus refinement map, EMD-7989 for the Ca^{2+}-bound CD focus refinement map, EMD-7991 for the full channel low IP_3-Ca^{2+} map, EMD-7993 for the low IP_3-Ca^{2+} TMD focus refinement map, EMD-7992 for the low IP_3-Ca^{2+} CD focus refinement map, EMD-7994 for the high IP_3-Ca^{2+} map, EMD-7995 for the high IP_3-Ca^{2+} TMD focus refinement map and EMD-7996 for the high IP_3-Ca^{2+} CD focus refinement map. Atomic coordinates are available from the RCSB Protein Data Bank under accession codes 6DQJ for the apo structure, 6DQN for IP_3 class 1, 6DQV for IP_3 class 2, 6DQS for IP_3 class 3, 6DQZ for IP_3 class 4, 6DR0 for IP_3 class 5, 6DR2 for the Ca^{2+}-bound structure, 6DRA for the low IP_3-Ca^{2+} structure and 6DBC for the high IP_3-Ca^{2+} structure.

Author contributions

N.P. and R.K.H. designed, performed and analyzed the experiments. N.P. and R.K.H. prepared the manuscript.

Competing financial interest statement

The authors declare no competing interests.

Introduction

Inositol trisphosphate receptors (IP_3R) are a family of large tetrameric Ca^{2+}-permeable cation channels predominantly expressed in the endoplasmic reticulum (ER)[1–5]. Three IP_3R subtypes exist in humans that share between 64 and 70% sequence identity but differ in their tissue expression and subcellular localization, resulting in homo- and heterotetrameric channels that perform a variety of physiological roles[6,7]. Activation of IP_3R by cytoplasmic Ca^{2+} and the second messenger inositol 1,4,5-trisphosphate (IP_3) allows Ca^{2+} to flow from the ER into the cytoplasm[2,8–11]. The dual regulation of IP_3R by Ca^{2+} and IP_3 integrates extracellular signaling pathways that lead to the generation of cytoplasmic IP_3 with intracellular Ca^{2+} signaling to jointly regulate the activity of numerous cellular processes including fertilization, differentiation, cell division and cell death[12–14]. Underscoring the essential role of these channels in diverse cell signaling pathways, the dysregulation of IP_3R is linked to cardiac disease, cancer, neurological disorders and other pathologies[6,15–19].

Electrophysiological and optical recordings of IP_3R activity in a variety of contexts have demonstrated that IP_3R displays a biphasic response to cytoplasmic Ca^{2+} (refs[9,18,20–22]). While low concentrations of cytoplasmic Ca^{2+} activate IP_3R, high concentrations of Ca^{2+} inhibit channel activity. The biphasic regulation of IP_3R by its permeant ion ensures precise spatiotemporal control of Ca^{2+} signaling. Depending on the input stimuli, IP_3R can generate cell-wide Ca^{2+} spikes or oscillatory waves as well as more localized Ca^{2+} “blips” or “puffs”[23–25]. Proper signal encoding requires Ca^{2+}-dependent inhibition as well as Ca^{2+}- and IP_3-dependent activation.

Despite intensive investigation into the regulation of IP_3R by Ca^{2+}, the mechanisms of Ca^{2+}-driven modulation remain open questions[26–29]. FRET experiments, partial proteolysis experiments, and negative-stain electron microscopic images suggest that Ca^{2+} stimulates large conformational changes, though the molecular details of these changes are unknown[30,31]. Analysis of single channel recordings suggest a high affinity activating Ca^{2+} site and a low affinity inhibiting Ca^{2+} site, though the residues that comprise these sites have yet to be identified[32]. In contrast, the molecular details of IP_3 binding to IP_3R have been better characterized. Mutational analysis identified the first ~600 residues of IP_3R as the IP_3-binding domain[3,33]. Crystal structures of isolated IP_3-binding domains in the presence and absence of IP_3 reveal that IP_3 binding is accompanied by a closing of the clamshell-like IP_3-binding domain around IP_3 (refs[34–37]). A cryo-electron microscopy (cryo-EM) structure of rat type 1 IP_3R (rIP_3R1) in a ligand-free state at a resolution of 4.7 Å revealed that this IP_3-binding domain is located more than 70 Å from the pore[38]. However, side-chain detail is lacking for most residues in the rIP_3R1 density map and the majority of the structural model was therefore built as a poly-alanine backbone. Thus, the architecture of IP_3R at atomic resolution remains unknown and it is unclear how IP_3 binding induces conformational changes that are propagated over such a long distance to influence the gating state of the pore. Therefore, high-resolution structural studies are required to understand the mechanisms through which Ca^{2+} and IP_3 regulate IP_3Rs. Here, we determined structures of full-length human type 3 IP_3R (hIP_3R3) in different states, allowing us to start to delineate the mechanistic basis for IP_3R regulation by IP_3 and Ca^{2+}.

Results

Architecture of ligand-free human type 3 IP_3 receptor

To resolve the atomic structure of a full-length human IP_3R, we first determined the structure of hIP_3R3 in a ligand-free state by single-particle cryo-EM at an overall resolution of 3.5 Å with C4 symmetry imposed (Supplementary Fig. 1 and Table 1). The map was of excellent quality, enabling us to *de novo* model most parts of the channel. However, some of the peripheral regions in the cytoplasmic domain and the carboxy-terminal domain were less well resolved. The density for the cytoplasmic domain was improved by employing symmetry expansion, signal subtraction and focused refinement[39] (Supplementary Fig. 1 and Supplementary Table 1). Using the cytoplasmic domain focused refinement map, we were able to build and register most of the cytoplasmic domain. In contrast, focused refinement approaches were unable to sufficiently improve the density for the small carboxy-terminal domain due to its extreme conformational flexibility. Thus, while the carboxy-terminal domain is present in the density map as a four-helix bundle as has been observed for rIP_3R1[38], it is not modeled in the final structure (Supplementary Fig. 2).

hIP_3R3 is a tetrameric channel comprised of 2671 residues per subunit with a large amino-terminal cytoplasmic domain (CD) followed by a juxtamembrane domain (JD) and a transmembrane domain (TMD), an architecture that resembles that of rIP_3R1[38] (Fig. 1a). Starting at the amino-terminus, the large CD can be divided into two β-trefoil-containing domains (BTF1, BTF2), an armadillo repeat domain (ARM1), the first segment of the central linker domain (CLD), a second armadillo repeat domain (ARM2), the second segment of the CLD and the third armadillo repeat domain (ARM3) (Supplementary Note 1). The CD is stabilized by a number of inter-subunit interactions including a central BTF ring that is composed of the BTF1 and BTF2 domains from all four subunits (Fig. 1b). The BTF ring, which contains several residues involved in IP_3 binding, is connected to the JD through the largely helical ARM1, CLD and ARM3 domains while the helical ARM2 domain is positioned at the periphery of the channel. The JD is comprised of the two segments that flank the TMD and is stabilized by a Zn^{2+} ion that is coordinated by Cys2538, Cys2541, His2558 and His2563. The Zn^{2+} binding site is also present in the structure of rIP_3R1 and in ryanodine receptor structures, indicating that the Zn^{2+}-binding site is broadly conserved[38,40].

While modeling the TMD, we noticed the presence of multiple hydrophobic lipid or detergent molecules forming a bilayer-like structure at the periphery of the TMD as well as two additional densities that could not be attributed to lipid molecules (Supplementary Fig. 3 and Supplementary Table 1). Inspection of these densities revealed that they correspond to two additional transmembrane helices located between the canonical S1 and S2 helices of the 6TM ion channel fold, which we will refer to as S1′ and S1″ (Fig. 1c). S1″ is positioned adjacent to S1 and S2 and is relatively well ordered in the density map, which allowed us to register its sequence. S1′ is positioned further from the S1–S4 domain on the outside of S1″ and is less well ordered in the density map. Focused classification and refinement improved the density for S1′, but the register could not be confidently determined and we thus modeled S1′ as an unregistered poly-alanine helix (Supplementary

Fig. 3). Sequence conservation of the region between S1 and S2 is high among the three human IP_3R types, especially within S1′. Indeed, close inspection of the rIP_3R1 density map revealed densities in similar positions as S1′ and S1″, suggesting that S1′ and S1″ are conserved features of IP_3Rs (Supplementary Fig. 3). S1′ and S1″ extend away from the channel in the membrane where they may potentially facilitate regulatory protein-protein interactions with other membrane-embedded proteins[41].

The ion conduction pathway of hIP_3R3 is formed by S5, S6 and the re-entrant pore helices of each subunit (Fig. 1d). Starting from the luminal side of the membrane, ions first pass through an electronegative vestibule formed by the extended loops between S5 and the pore helix and between the pore helix and S6. A total of 12 negatively charged residues (Glu2398, Asp2400 and Asp2478 from each subunit) are resolved in the luminal vestibule. The electronegative environment of the vestibule may serve to concentrate cations before entering the pore, potentially facilitating Ca^{2+} conductance. Two constrictions are present in the pore between the luminal vestibule and cytoplasmic opening. The first constriction is created by the backbone carbonyl oxygen of Asn2472, which resides on the pore helix (Fig. 1d and Fig. 1e). The constriction has a radius of about 3 Å at its narrowest point and along with neighboring residues may contribute to ion selectivity, although IP_3R3 is only weakly selective for Ca^{2+} over other cations[42]. The second constriction is a hydrophobic gate formed by the side chains of Phe2513 and Ile2517 of S6, which constricts the pore to a radius of less than 1 Å, too narrow to conduct Ca^{2+}. The ligand-free state of hIP_3R3 is thus a non-conductive state, consistent with electrophysiological recordings showing that Ca^{2+} and IP_3 are required for IP_3R activation[2,18,32].

IP_3-bound conformations

To resolve the conformational changes associated with IP_3 binding in the context of the full channel, we collected images of hIP_3R3 in the presence of saturating (50 μM) IP_3. Successive rounds of three-dimensional classification revealed an ensemble of distinct IP_3-bound conformational states (Supplementary Fig. 4). Five of the conformational states were sufficiently well populated to generate 3D reconstructions at resolutions up to 3.3 Å, from which we could model their structures.

A reconstruction of the particles assigned to the first class, IP_3 class 1, at 3.3 Å revealed an overall conformation that is similar to the apo state (Fig. 2a and Table 1). The structure of IP_3 class 1 has an all-atom RSMD of approximately 1 Å compared to the apo structure. Despite this overall structural similarity, local conformational changes are present in the IP_3-binding domain. The ARM1-proximal region of BTF2 moves 4 Å towards ARM1 in IP_3 class 1, narrowing the interface between the two domains without disrupting the BTF ring. In the interface between BTF2 and ARM1, we identified a three-lobed density that we modeled as an IP_3 molecule (Supplementary Fig. 5). The IP_3 molecule is coordinated by the positively charged side chains of Arg266 and Arg270 from BTF2 and Arg503, Lys507, Arg510, Arg568 and Lys569 from ARM1 (Fig. 2b and Supplementary Fig. 5), many of which have been previously identified as residues that directly bind IP_3 in crystal structures of isolated IP_3-binding domains[34,36,37].

Whereas IP_3 class 1 closely resembles apo hIP_3R3, a reconstruction of the particles assigned to IP_3 class 2 at 3.8 Å reveals significant conformational changes (Supplementary Fig. 4 and Table 1). Compared to the apo structure, the length of IP_3 class 2 is 5 Å shorter along the four-fold axis and the conformation of the CD is substantially different (Fig. 2d). To better understand the origin of these conformational changes, we examined the IP_3-binding site of class 2. Similar to class 1, an IP_3 molecule is coordinated by the side chains of Arg266, Arg270, Arg503, Lys507, Arg510, Arg568 and Lys569 from BTF2 and ARM1 (Fig. 2e and Supplementary Fig. 5). However, the configuration of the IP_3-binding domain differs in class 2. In class 2, IP_3 binding is accommodated by a rigid-body rotation of ARM1 towards BTF2, which adopts an apo-like conformation (Fig. 2e). The only changes in BTF2 compared to the apo state are slight movements of the loops that directly coordinate IP_3.

Because ARM1 moves relative to the fixed BTF ring structure in IP_3 class 2, IP_3 binding is accompanied by conformational changes throughout the channel (Fig. 2d). These conformational changes can be separated into two major movements. The first is a coupled movement of the CLD and ARM3 that results in a 5° rotation of the JD (Fig. 2f, Supplementary Video 1 and Supplementary Video 2). While the TMD is nearly unchanged relative to the apo state, these concerted movements provide a model for how ligand binding can be transmitted through multiple helical domains to the pore. The second conformational change is a 17 Å movement of ARM2 to position itself near the CLD of the same subunit (Fig. 2d, Supplementary Video 1 and Supplementary Video 2). Besides coming nearly into contact with the CLD, the movement of ARM2 also alters its interactions with the neighboring subunit. ARM2 no longer makes contacts with ARM1 of the neighboring subunit and its interaction with BTF2 of the neighboring subunit is shifted by 2 armadillo repeats from α63 to α68.

When examining the density maps of IP_3 classes 3, 4 and 5, we realized that they are not four-fold symmetric like the maps of classes 1 and 2 (Supplementary Fig. 4). The asymmetry of these classes is most apparent in the positions of the four ARM2 domains, which can adopt either a class 1-like extended conformation or a class 2-like compact conformation (Fig. 3a). We therefore calculated reconstructions of classes 3, 4 and 5 without imposing symmetry at resolutions of 4.1, 6.0 and 4.5 Å, respectively (Table 1). Structures of classes 3, 4 and 5 were initially modeled by rigid-body docking domains of classes 1 or 2 into the density map and then comparing which of the two structures fit best into the density map. The docking demonstrated that these classes were composed of both class 1-like and class 2-like domains (Fig. 3b).

Even at the moderate resolutions of these reconstructions, inspection of the IP_3-binding domains reveals densities consistent with IP_3 molecules at the BTF2-ARM1 interfaces in all three density maps (Supplementary Fig. 5). Thus, the asymmetry in these classes is not caused by variations in IP_3-binding site occupancies. Rather, the asymmetry arises from variations in the conformation of the individual subunits. Notably, a single subunit can be composed of domains that adopt class 1-like and domains that adopt class 2-like conformations. For example, one of the subunits in class 5 has a class 1-like IP_3-binding domain, while the rest of the subunit is class 2-like (Fig. 3b).

Thus, despite IP_3R possessing a single IP_3 binding site, the configuration of the IP_3-binding domain can vary when IP_3 is bound and these variations are coupled to large changes in global channel conformation (Fig. 2). Notably, both configurations can be present in the same channel indicating that the binding modes are in dynamic exchange and that stable intermediates exist between them (Fig. 3). Multiple crystal structures have been determined of isolated IP_3-binding domains in complex with IP_3 (refs[34,36,37]). The position of ARM1 relative to BTF2 varies among these structures, adopting a range of conformations between those present in IP_3 class 1 and IP_3 class 2 suggesting that the rest of the channel may influence the configuration of the IP_3-binding domain (Supplementary Fig. 5).

Ca^{2+}-bound conformations

To identify the Ca^{2+} binding sites and visualize the effects of Ca^{2+} binding on IP_3R conformation, we next determined a structure of hIP_3R3 at 4.3 Å resolution in the presence of approximately 2 mM Ca^{2+} with C4 symmetry imposed, which we will refer to as Ca^{2+}-bound (Supplementary Fig. 6 and Table 1). Examination of the map revealed that the peripheral portions of the CD, including BTF1, BTF2 and ARM1 were poorly resolved and not strictly four-fold symmetrical. We therefore employed two different focused refinement strategies to better resolve the channel. We first calculated a four-fold symmetric reconstruction of ARM3, the JD and the TMD to a resolution of 4.2 Å (Supplementary Fig. 6 and Supplementary Table 1). Next, to improve the density of the flexibly attached CD, we employed signal subtraction, symmetry expansion and focused refinement, resulting in a 4.7 Å reconstruction in which the CD is clearly resolved (Supplementary Fig. 6 and Supplementary Table 1). The structure of Ca^{2+}-bound hIP_3R3 was modeled using both the full channel and focused refinement maps. In addition to densities corresponding to hIP_3R3, both the full channel and focused refinement maps contained densities corresponding to two bound Ca^{2+} ions per subunit (Fig. 4a and Supplementary Fig. 7). The first Ca^{2+}, which we will call the CD Ca^{2+}, is located at the interface between CLD and ARM2 where it is coordinated by main-chain and side-chain oxygen atoms from both domains (Fig. 4a,b). The CLD contributes the main-chain carbonyl oxygen of Arg743, while ARM3 contributes the side chain of Glu1125 and the main-chain carbonyl oxygen of Glu1122. From the apo state, ARM2 moves 28 Å to complete the binding site (Fig. 4c). Notably, ARM2 in the Ca^{2+}-bound state is in a similar conformation to its location in IP_3 class 2. From its position in IP_3 class 2, Glu1122 and Glu1125 on ARM2 must move only an additional 3 Å to complete the coordination of the CD Ca^{2+}. The second Ca^{2+}, which we will refer to as the JD Ca^{2+}, occupies a cavity between the JD and ARM3 (Fig. 4a and Supplementary Fig. 7). The JD Ca^{2+} is coordinated by the side chains of two glutamate residues on ARM3 (Glu1882 and Glu1946) and by main-chain and side-chain carbonyl oxygens of one residue on the JD (Thr2581) (Fig. 4d). To bring the side chains of Glu1882 and Glu1946 into close proximity of Thr2581 and complete the Ca^{2+} coordination, ARM3 must rotate 11° compared to the apo state (Fig. 4e). In the Ca^{2+}-bound conformation, the structure of the JD binding site almost perfectly matches that of a Ca^{2+} binding site identified in the rabbit ryanodine receptor structure suggesting that some aspects of channel regulation are conserved between IP_3Rs and ryanodine receptors[40] (Supplementary Fig. 7d).

Figure 5 shows a comparison of the tetrameric Ca^{2+}-bound and apo structures revealing the conformational changes induced by Ca^{2+} binding at the CD and JD sites. The most obvious differences between the structures are a nearly 30 Å dilation of the CD and a complete disruption of the BTF ring that anchors inter-subunit interactions (Fig. 5 and Supplementary Video 3). Indeed, close inspection reveals that Ca^{2+} binding eliminates all of the inter-subunit interactions present in the apo and the IP_3-bound structures. Dissociation of the CDs yields a channel in which the four CDs are physically uncoupled from one another, explaining the increased mobility of the CDs compared to the apo state. The dissociation also explains the reduced retention time of Ca^{2+}-bound hIP_3R in gel filtration experiments compared to unliganded channels and is consistent with FRET measurements demonstrating global conformational changes in the presence of Ca^{2+} (ref[31]) (Supplementary Fig. 6a).

Ca^{2+}- and IP_3-bound conformations

To understand how IP_3 and Ca^{2+} coordinate to regulate channel gating, we determined structures of hIP_3R3 in the presence of approximately 2 mM Ca^{2+} and either 10 μM (low) or 50 μM (high) IP_3 at 4.0 Å and 3.9 Å, respectively (Supplementary Fig. 8, Supplementary Fig. 9 and Table 1). Similar to the Ca^{2+}-bound state, the CD was poorly ordered in both the low IP_3-Ca^{2+} and high IP_3-Ca^{2+} reconstructions. We therefore calculated two sets of focused refinement maps for each condition. The TMD focused refinement maps were resolved to 3.8 Å for the low IP_3-Ca^{2+} state and 3.7 Å for the high IP_3-Ca^{2+} state while the CD focused refinement maps were resolved to 4.2 Å for the low IP_3-Ca^{2+} state and 3.8 Å for the high IP_3-Ca^{2+} state (Supplementary Figure 8, Supplementary Figure 9, Supplementary Table 1). Inspection of the ligand-binding sites in the high IP_3-Ca^{2+} condition revealed density consistent with the IP_3-binding site and both Ca^{2+} sites being occupied (Supplementary Fig. 10). To bind IP_3, ARM1 in the high IP_3-Ca^{2+} condition is rotated 15° towards BTF2 to adopt a conformation that is similar to IP_3 class 2. In the low IP_3-Ca^{2+} condition densities are clearly present at both of the Ca^{2+} sites, but the IP_3-binding site is unoccupied and the IP_3-binding domain adopts an apo-like conformation.

Despite IP_3 being bound, the overall structure of the high IP_3-Ca^{2+} state closely resembles the Ca^{2+}-bound structure (Fig. 6a,c and Supplementary Video 3). In both structures the BTF rings are dissociated and the four CDs are detached from one another. Indeed, the only difference in the high IP_3-Ca^{2+} structure compared to the Ca^{2+}-bound structure is a clamping down of the IP_3-binding domain around IP_3. In contrast to the similarity between the Ca^{2+}-bound and high IP_3-Ca^{2+} structures, the structure of IP_3 class 2 demonstrates that global conformational changes can occur following IP_3 binding (Fig. 6b,d). Whereas the network of inter-subunit interactions in the cytoplasmic domain enable conformational changes to be propagated throughout the channel in IP_3 class 2, their disruption in the high IP_3-Ca^{2+} structure results in four CDs that are physically uncoupled from one another and from the pore. Thus, the Ca^{2+} binding sites stabilize the high IP_3-Ca^{2+} structure in an inhibited conformation. Furthermore, Ca^{2+} binding also stabilizes the separation of the CD domains in the low IP_3-Ca^{2+} and Ca^{2+}-bound structures indicating that Ca^{2+}-dependent IP_3R inhibition may be independent of IP_3-binding state (Fig. 5).

Discussion

The ensemble of structures presented here outlines a model for how IP_3 and Ca^{2+} control the gating of IP_3R. The structures support a model in which a network of inter-subunit interactions enables the propagation of conformational changes from peripheral ligand binding domains to the JD and TMD. It has long been recognized that domains such as BTF1, which do not directly contribute to ligand binding, are essential for IP_3R gating[42–45]. The IP_3-bound structures demonstrate that these domains are essential because of their incorporation into the inter-subunit interactions network. BTF1, for example, is a key component of a central ring structure that serves to anchor the inter-subunit network and forms a fulcrum against which movements of the IP_3-binding domain are propagated throughout the channel. Thus, this network ensures that conformational changes in the IP_3-binding domain are coupled to the gating state of the pore (Fig. 2). Ca^{2+} binding disrupts this network leading to an inhibited state where movements due to IP_3 binding are insulated from global channel conformation (Fig. 6).

While high concentrations of Ca^{2+} inhibit IP_3R, low concentrations of Ca^{2+} are required for activation. In the Ca^{2+}-bound inhibited structures two Ca^{2+} ions are present: one in the periphery of the CD (CD Ca^{2+}) and one at the CD-JD interface (JD Ca^{2+}). The presence of two Ca^{2+} binding sites at distinct locations within IP_3R is consistent with different apparent Ca^{2+} binding affinities for activation and inhibition[32]. While the functional role of the two sites cannot be distinguished from the structural data alone, it is possible that the two sites play distinct roles in gating, with one regulating IP_3R activation and the second inhibition.

Aligning the structures into a trajectory allows us to posit a model for how IP_3 and Ca^{2+} binding leads to activation of hIP_3R3 (Fig. 7). Due to the similarity between the apo state and IP_3 class 1, we hypothesize that upon IP_3 binding the channel first adopts a structure similar to IP_3 class 1 in which conformational changes are limited to the local environment of the IP_3-binding domain. Spontaneous rearrangements of individual IP_3-binding domains into class 2-like configurations may then allow the channel to adopt asymmetric intermediate conformations analogous to IP_3 classes 3, 4 and 5 in which subunits within the channel can adopt different conformations. The presence of multiple stable intermediate states suggests that the conformational exchange between the two IP_3-binding domain configurations occur on a per-subunit basis rather than as a concerted mechanism in which all four subunits act as one (Fig. 3). Compared to the apo state, ARM3 and the JD are rotated as more of the IP_3-binding domains adopt the IP_3 class 2-like configuration suggesting that IP_3-bound structures are intermediates on the pathway to activation (Fig. 2 and Fig. 3). We speculate that Ca^{2+} binding at one of the sites may induce further rotation of the JD leading to an opening of the S6 gate and a conductive state. Between the selectivity filter and the S6 gate, a portion of S6 adopts a short five-turn or π-helical region in the apo structure. Relaxation from this high-energy π-helix into a lower energy α-helix upon JD rotation may help to stabilize the pore in a conductive state. Transitions between π-helical and α-helical conformations within the S6 helices during gating have been recently described in TRPV6[46]. It is also possible that all of the IP_3-bound states can directly access an activated state. Single-channel recordings have identified three reversible modes with distinct gating kinetics whose open channel probability vary by more than 100-fold without changing Ca^{2+}

or IP_3 concentrations[47]. These gating modes may result from the existence of different IP_3-bound states that open with stably different probabilities. IP_3 class 1, which is nearly identical to the apo state, would require large conformational changes and despite the presence of bound IP_3 may be the least likely to open. In contrast, IP_3 class 2, in which IP_3 binding is accompanied by conformational changes that propagate towards the pore, may be more likely to open. Thus, the ensemble of structures provide a foundation for beginning to understand the complex gating of IP_3Rs.

Online Methods

Cell Lines

HEK293S GnTI- (human embryonic kidney, N-acetylglucosaminyltransferase I knockout) cells were used for protein expression and maintained in Freestyle 293 Expression Media (Gibco) supplemented with 2% fetal bovine serum (FBS) at 37˚ C.

Constructs

A gene for human type 3 IP_3R (HsITPR3) in pENTR223 vector was obtained from HMS PlasmID (HsCD00399229). Internal restriction sites for XhoI and EcoRI were removed by site directed mutagenesis. Polymerase chain reaction (PCR) was used to amplify the gene and add restriction sites for XhoI and EcoRI for in-frame subcloning into a bacmam expression vector with an N-terminal GFP and PreScission protease cut site[48,49]. The final product (N-GFP-HsITPR3) was sequenced in its entirety.

hIP$_3$R3 Expression & Purification

N-GFP-HsITPR3 was used to transform DH10Bac E. coli cells to generate bacmid DNA. Recombinant baculovirus was produced by three rounds of viral amplification in Sf9 (Spodoptera frugiperda) cells maintained in Grace’s media supplemented with 10% FBS, 1% penicillin/streptomycin, and 0.1% Pluronic F-68. Viral particles were separated from cell debris by centrifugation and filtration, and used to infect HEK293S GnTI- cells for protein production. For the first 24 hours of infection, cultures were grown at 37˚ C, after which sodium butyrate was added to a final concentration of 10 mM and cells moved to 30˚ C to grow for an additional 48–72 hours prior to harvesting. Cell pellets were washed in phosphate-buffered saline solution and flash frozen in liquid nitrogen.

Thawed cell pellets were solubilized for 1 hour in 2% lauryl maltose neopentyl glycol, 4 mM cholesterol hemisuccinate (CHS), 20 mM HEPES pH 7.5, 150 mM NaCl with protease inhibitor cocktail (1 mM PMSF, 2.5 ug/mL aprotinin, 2.5 ug/mL leupeptin, 1 ug/mL pepstatin A, 0.5 mM AEBSF, 1 mM benzamidine), and DNAse. Whole cell lysates were centrifuged at 75,000xg for 40 minutes, and the soluble fraction was bound to GFP-nanobody beads for 1–3 hours on a rotator[50]. Beads were collected on a column by gravity and then washed with 50 mL of wash buffer (150 mM NaCl, 50 mM Tris pH 8.0, 2 mM DTT, 0.06% digitonin). The protein was digested with PreScission protease diluted in wash buffer on the column for 3 hours to separate the channel from the GFP and then eluted with 12 mL of wash buffer.

Concentrated protein was further purified by size-exclusion chromatography on a Superose 6 Increase (GE Life Sciences) column in gel filtration buffer (150 mM NaCl, 50 mM Tris pH 8.0, 2 mM DTT, 0.06% digitonin) with either addition of 100 μM Ca^{2+}, 1 mM Ca^{2+}, 5 mM EGTA or 10 mM HEDTA, based on the conditions required for vitrification. Peak fractions were pooled and concentrated to ~8 mg/mL for cryo-EM analysis. For cryo-EM samples containing IP_3 (d-*myo*-Inositol 1,4,5-Trisphosphate), a stock solution of 1 mM IP_3 (Calbiochem, SR5440-1102-669) in ddH2O was added to bring the solution to the appropriate concentration approximately 30 minutes before vitrification.

Electron Microscopy Sample Preparation and Imaging

3.5–5 μl of purified channel at a concentration of ~8 mg/mL was pipetted onto glow-discharged 400 mesh gold Quantifoil R1.2/1.3 holey carbon grids (Quantifoil, Q25869) approximately 5–20 seconds before blotting (blot force = 1) for two seconds and plunging into liquid nitrogen-cooled liquid ethane using an FEI Vitrobot Mark IV (FEI ThermoFisher). Precise control over free Ca^{2+} concentrations in the vitrified samples is complicated by the presence of high concentrations of Ca^{2+} in the filter paper used for blotting excess solution away from the grid. Prior to our data collection, we performed initial screening experiments using various Ca^{2+} and EGTA concentrations, which suggested that the final concentration of free Ca^{2+} may be as much as 2 mM higher than those used during sample preparation. This estimate was based upon the concentrations of Ca^{2+} and EGTA needed to completely eliminate the inhibited conformation. Efforts to more precisely estimate the free Ca^{2+} following blotting were complicated by the extremely small quantity of solution remaining on the grid following blotting (less than 0.01 μl). The Ca^{2+} concentrations presented here are thus best estimates and may not reflect the true concentration of free Ca^{2+} to which the samples are exposed. Additional conditions were tested, but the presence of channels in Ca^{2+}-inhibited states indicated that the free Ca^{2+} was not well controlled. For the ligand-free condition, we added no free Ca^{2+} and either 5 mM EGTA or 10 mM HEDTA and predict a free Ca^{2+} below 100 nM. For the IP_3-bound condition, we added no free Ca^{2+} and 5 mM EGTA and predict a free Ca^{2+} below 100 nM. For the Ca^{2+}-bound condition, we added 1 mM Ca^{2+} and no EGTA and predict a free Ca^{2+} above 1 mM. For the low IP_3-Ca^{2+} condition, we added 100 μM Ca^{2+} and no EGTA and predict a free Ca^{2+} above 1 mM. For the high IP_3-Ca^{2+} condition, we added 100 μM Ca^{2+} and no EGTA and predict a free Ca^{2+} above 1 mM.

Grids were transferred to an FEI Titan Krios cryo-EM operating at 300 kV. Images were recorded in an automated fashion using SerialEM or Leginon with a defocus range of −1.0 to −2.5 μM over 8 seconds as 40 sub-frames using a Gatan K2 Summit direct electron detector in super-resolution mode[51,52]. For the apo data collection, images were recorded at a calibrated super-resolution pixel size of 0.548 Å/pixel with energy filter slit width of 20 eV. For all other data sets, images were recorded at a calibrated super-resolution pixel size of 0.544 Å/pixel. Electron dose was 9 e^-/pix/s at the detector for a total accumulated dose of 60 $e^-/Å^2$ for the apo data set and 61 $e^-/Å^2$ for the other data sets. Images were two-times Fourier cropped and aligned using whole frame and local correction algorithms by Motioncor2 resulting in a final calibrated pixel size of 1.096 Å/pixel for the apo data set and 1.088 Å for the other data sets[53]. The effects of the contrast transfer function were estimated

using CTFfind 4.1.8 (ref[54]). A total of 1801, 4795, 944, 1409, and 4076 images were recorded for the apo, IP_3-bound, Ca^{2+}-bound, low IP_3-Ca^{2+} and high IP_3-Ca^{2+} data sets, respectively. After removing images with excessive drift, bad ice or poor contrast, 1767, 4519, 926, 1409, and 3974 images were kept for processing for the apo, IP_3-bound, Ca^{2+}-bound, low IP_3-Ca^{2+} and high IP_3-Ca^{2+} data sets, respectively.

Cryo-EM analysis

Approximately 1000 particles from each data set were manually selected to generate initial templates for autopicking using Relion[39]. Several rounds of 2D classification and autopicking were used to generate improved templates for autopicking. An initial model of the apo condition was generated from the autopicked particles using CryoSPARC[55] and used as the starting model for all data sets. Two-dimensional and three-dimensional classification in Relion were used to eliminate false-positives or damaged particles resulting in 53k, 303k, 49k, 74k, and 170k images for the apo, IP_3-bound, Ca^{2+}-bound, low IP_3-Ca^{2+} and high IP_3-Ca^{2+} data sets, respectively. The particle images were polished in Relion to realign particles on a per-particle basis and correct for dose-dependent beam-induced specimen damage.

For the apo condition, the polished particle stack was subjected to one round of three-dimensional classification resulting in a particle stack of 26k homogenous particles. For refinement, the particles were analyzed by cisTEM with C4 symmetry imposed[56]. For the initial global search in cisTEM, the reference map generated in Relion was filtered to 20 Å. For the final iterations, the references were filtered to 5 Å. Using the 0.143 FSC criterion, the resolution was estimated to be 3.49 Å[57].

To improve the features of the CLD and ARM2 in the apo reconstruction, the stack of 53k particles was subjected to focused three-dimensional classification, resulting in a stack of 30k particles that was symmetry expanded to 120k particles in C1 and the signal was subtracted for the CD and JD of three of the subunits, and the entire TMD. Focused refinement in Relion using a soft mask that included only the CD and JD of one subunit resulted in a reconstruction whose resolution was estimated to be 3.76 Å by the 0.143 FSC criterion.

To improve the features of S1′ and S1″ in the apo reconstruction, the stack of 30k particles was symmetry expanded to 120k particles in C1 and the signal was subtracted for the CD of three of the subunits. Focused refinement in Relion using a soft mask that included the TMD and JD of all four subunits and the CD of one subunit followed by focused classification using a mask that just included the S1–S4 domain of one subunit yielded one major class (81k particles) in which S1′ and S1″ were improved. Focused refinement in Relion of the 81k particles using a soft mask that just included the TMD and JD and all four subunits and the CD of one subunit resulted in a reconstruction whose resolution was estimated to be 3.69 Å by the 0.143 FSC criterion.

For the IP_3 condition, the stack of 303k polished particles was subjected to one round of three-dimensional classification specifying 7 classes without imposing symmetry using a reference in which the four ARM2 domains had been removed. After the first round, one class was poorly resolved (40k particles) and excluded from later processing steps. The

remaining particles were merged into 3 groups based upon the positions of the ARM2 domain and reclassified using a reference lacking the ARM2 domains into 7 classes without imposing symmetry. After the second round, the classes were merged into 5 groups based upon the positions of the ARM2 domain. The particles were then reclassified and merged two additional times. The merged particle stacks were then refined without symmetry and classified without angular sampling to remove any misclassified particles. The final cleaned particle stacks were then refined in cisTEM. Classes 1 (39k particles) and 2 (41k particles) were refined in cisTEM with C4 symmetry. For the initial global search in the refinement of classes 1 and 2 in cisTEM, the reference maps generated in Relion were filtered to 20 Å. For the final iterations, the references were filtered to 4.8 Å for class 1 and 6 Å for class 2. Using the 0.143 FSC criterion, the resolutions were estimated to be 3.33 Å for class 1 and 3.82 for class 2. Classes 3, 4 and 5 were refined in cisTEM without symmetry. For the initial global search of classes 3 (38k particles), 4 (10k particles) and 5 (27k particles) in cisTEM, the reference map generated in Relion was filtered to 20 Å. For the final iterations, the references were filtered to 6, 10 and 7 Å, for classes 3, 4 and 5 respectively. Using 0.143 FSC criterion, the resolutions for classes 3, 4 and 5 were estimated to 4.12, 6.01 and 4.47 Å, respectively.

For the Ca^{2+}-bound condition, the polished particle stack was subjected to one round of focused three-dimensional classification using a soft mask including ARM3, the JD and the TMD with C4 symmetry imposed resulting in a final particle stack of 34k particles. The particle stack was analyzed in cisTEM with C4 symmetry imposed. For the initial global search in cisTEM, the reference map generated in Relion was filtered to 20 Å. For the final iterations, the references were filtered to 7 Å. Using the 0.143 FSC criterion, the resolution was estimated to be 4.33 Å. To improve the alignment of the more rigid ARM3, JD and TMD, which includes the JD Ca^{2+} binding site, a soft mask was applied to those domains during refinement in Relion, yielding a reconstruction at 4.2 Å. To improve the features of the CD, the stack of 34k particles was symmetry expanded to 135k particles in C1 and the signal was subtracted for the CD of three of the subunits. Focused refinement in Relion using a soft mask including the TMD and JD of all four subunits and the CD of one subunit resulted in a reconstruction whose resolution was estimated to be 4.69 Å by the 0.143 FSC criterion.

For the low IP_3-Ca^{2+} condition, the polished particle stack of 74k particles was classified into 6 classes without imposing symmetry. Four of the six classes, totaling 49k particles, were selected for refinement in cisTEM with C4 symmetry imposed. For the initial global search in cisTEM, the reference map generated in Relion was filtered to 20 Å. For the final iterations, the references were filtered to 7 Å. Using the 0.143 FSC criterion, the resolution was estimated to be 3.96 Å. To improve the alignment of the more rigid ARM3, JD and TMD, which includes the JD Ca^{2+} binding site, a soft mask was applied to those domains during refinement in Relion, yielding a reconstruction at 3.80 Å. To improve the features of the CD, the stack of 196k particles was symmetry expanded to C1 and the signal was subtracted for the JD and CD of three of the subunits, and the entire TMD. Focused classification in Relion using a soft mask that included the JD and CD of one subunit yielded a single major class of 158k particles. Refinement of the 158k particles in Relion using a

soft mask that included the JD and CD of one subunit resulted in a reconstruction whose resolution was estimated to be 4.22 Å by the 0.143 FSC criterion.

For the high IP_3-Ca^{2+} condition, the polished particle stack of 170k particles was analyzed in cisTEM with C4 symmetry imposed. One round of three-dimensional classification into seven classes identified six similar classes containing a total of 131k particles. Refinement of these 131k particles in cisTEM resulting in a reconstruction with an estimated resolution of 3.92 Å using reference filtered to 7 Å. To improve the alignment of the more rigid ARM3, JD and TMD, which includes the JD Ca^{2+} binding site, a soft mask was applied to those domains during classification and refinement in Relion, yielding a reconstruction at 3.66 Å. To improve the features of the CD, the stack of 170k particles was symmetry expanded to C1 and the signal was subtracted for the CD of three of the subunits. Focused classification identified a population of 350k particles that when refined in cisTEM using a soft mask that included the JD and CD of one subunit resulted in a reconstruction whose resolution was estimated to be 3.78 Å by the 0.143 FSC criterion.

Model building and coordinate refinement

The structure of ligand-free IP_3-binding domain of rIP_3R1 (PDB: 3UJ4)[37] was docked into the full channel apo state density map using UCSF Chimera[58] and then manually rebuilt according to the density in Coot[59]. The remainder of the protein was built *de novo* into the apo state full channel, apo state CD focused refinement and S1–S4 focused refinement density maps. The refined apo state model contains residues 5-80, 85-321, 350-527, 534-674, 690-893, 961-1003, 1024-1036, 1043-1129, 1167-1432, 1587-1687, 1717-1804, 1863-2038, 2043-2074, 2111-2226, 2260-2403 and 2449-2611. Unregistered poly-alanine helices were modeled for S1′ and α71-α75 at the C-terminal end of ARM2 using Jpred4[60]. The coordinates were refined against one of the full-channel half-maps (work) using Rosetta 3.7[61] and phenix.real_space_refine[62] with secondary structure and Ramachandran restraints maintained throughout. To monitor the effects of over fitting during coordinate refinement, Fourier shell correlations were compared against the half-map excluded from refinement (free). Map to model correlations were determined using phenix.mtriage (https://www.phenix-online.org/newsletter/CCN_2017_07.pdf).

For IP_3 classes 1 and 2 and the Ca^{2+}-bound structures, the final refined model of apo hIP_3R was docked into the density map using UCSF Chimera and then manually rebuilt according to the density in Coot. The coordinates were refined against one of the full-channel half-maps (work) using phenix.real_space_refine with secondary structure and Ramachandran restraints maintained throughout. To monitor the effects of over fitting during coordinate refinement, Fourier shell correlations were compared against the half-map excluded from coordinate refinement (free). Map to model correlations were determined using phenix.mtriage.

For IP_3 classes 3, 4 and 5, the refined models of IP_3 classes 1 and 2 were docked into the density on a subunit-by-subunit basis by rigid-body fitting in coot. Once the overall fit of the models were completed, the models of IP_3 classes 1 and 2 were split into domain fragments and docked into the density map by rigid-body fitting. The rigid-body fit model was refined by real-space refinement for classes 3 and 5 in phenix.real_space_refine against one of the

half-maps and rigid-body refinement for class 4 in phenix.real_space_refine against the full reconstruction.

Software was compiled by SBGrid[63]. Local resolution estimates were performed using ResMap[64] and structure figures were prepared with UCSF Chimera and PyMol (PyMol version 1.8.0 Schrodinger LLC).

Data availability

Cryo-EM maps have been deposited in the EMDB under accession codes EMD-7978 for the full channel apo map, EMD-7979 for the apo CD focus refinement map, EMD-7980 for the apo S1–S4 focus refinement map, EMD-7981 for the IP_3 class 1 map, EMD-7982 for the IP_3 class 1 CD focus refinement map, EMD-7984 for the IP_3 class 2 map, EMD-7982 for the IP_3 class 2 CD focus refinement map, EMD-7985 for the IP_3 class 3 map, EMD-7986 for the IP_3 class 4 map, EMD-7987 for the IP_3 class 5 map, EMD-7888 for the full channel Ca^{2+}-bound map, EMD-7990 for the Ca^{2+}-bound TMD focus refinement map, EMD-7989 for the Ca^{2+}-bound CD focus refinement map, EMD-7991 for the full channel low IP_3-Ca^{2+} map, EMD-7993 for the low IP_3-Ca^{2+} TMD focus refinement map, EMD-7992 for the low IP_3-Ca^{2+} CD focus refinement map, EMD-7994 for the high IP_3-Ca^{2+} map, EMD-7995 for the high IP_3-Ca^{2+} TMD focus refinement map and EMD-7996 for the high IP_3-Ca^{2+} CD focus refinement map. Atomic coordinates are available from the RCSB Protein Data Bank under accession codes 6DQJ for the apo structure, 6DQN for IP_3 class 1, 6DQV for IP_3 class 2, 6DQS for IP_3 class 3, 6DQZ for IP_3 class 4, 6DR0 for IP_3 class 5, 6DR2 for the Ca^{2+}-bound structure, 6DRA for the low IP_3-Ca^{2+} structure and 6DBC for the high IP_3-Ca^{2+} structure. All other source data are available from the corresponding author upon request.

Supplementary Material

Refer to Web version on PubMed Central for supplementary material.

Acknowledgments

We thank M. de le Cruz at the Memorial Sloan Kettering Cancer Center Cryo-EM facility and staff at the New York Structural Biology Simons Electron Microscopy Center for help with data collection and S.B. Long and T. Walz for comments on the manuscript. This work was supported in part by National Institutes of Health grant CA008748, the Josie Robertson Investigators Program and the Searle Scholars Program.

References

1. Burgess GM, Mckinney JS, Fabiatoq A, Leslie BA, Putney JW. Calcium Pools in Saponin-permeabilized Guinea Pig Hepatocytes. J Biol Chem. 1983; 258:35336–153345.
2. Ehrlich BE, Watras J. Inositol 1,4,5-trisphosphate activates a channel from smooth muscle sarcoplasmic reticulum. Nature. 1988; 336:583–586. [PubMed: 2849060]
3. Furuichi T, et al. Primary structure and functional expression of the inositol 1,4,5-trisphosphate-binding protein P400. Nature. 1989; 342:32–38. [PubMed: 2554142]
4. Mignery GA, Südhof TC, Takei K, De Camilli P. Putative receptor for inositol 1,4,5-trisphosphate similar to ryanodine receptor. Nature. 1989; 342:192–5. [PubMed: 2554146]
5. Streb H, Irvine RF, Berridge MJ, Schulz I. Release of Ca2+from a nonmitochondrial intracellular store in pancreatic acinar cells by inositol-1,4,5-trisphosphate. Nature. 1983; 306:67–69. [PubMed: 6605482]

6. Foskett JK, White C, Cheung KH, Mak DOD. Inositol trisphosphate receptor Ca2+ release channels. Physiol Rev. 2007; 87:593–658. [PubMed: 17429043]
7. Vervloessem T, Yule DI, Bultynck G, Parys JB. The type 2 inositol 1,4,5-trisphosphate receptor, emerging functions for an intriguing Ca^{2+}-release channel. Biochimica et biophysica acta. 2015; 1853:1992–2005. [PubMed: 25499268]
8. Ferris CD, Huganir RL, Supattapone S, Snyder SH, Solomon H. Purified inositol 1,4,5-trisphosphate receptor mediates calcium flux in reconstituted lipid vesicles. Nature. 1989; 342:87–9. [PubMed: 2554143]
9. Finch EA, Turner TJ, Goldin SM. Calcium as a coagonist of inositol 1,4,5-trisphosphate-induced calcium release. Science. 1991; 252:443–446. [PubMed: 2017683]
10. Jean T, Klee CB. Calcium modulation of inositol 1,4,5-trisphosphate-induced calcium release from neuroblastoma x glioma hybrid (NG108-15) microsomes. J Biol Chem. 1986; 261:16414–16420. [PubMed: 3491073]
11. Suematsu E, Hirata M, Hashimoto T, Kuriyama H. Inositol 1,4,5-trisphosphate releases Ca2+from intracellular store sites in skinned single cells of porcine coronary artery. Biochem Biophys Res Commun. 1984; 120:481–485. [PubMed: 6610416]
12. Armant DR. Intracellular Ca2+ signaling and preimplantation development. Adv Exp Med Biol. 2015; 843:151–171. [PubMed: 25956298]
13. Berridge MJ. Calcium signalling remodelling and disease. Biochem Soc Trans. 2012; 40:297–309. [PubMed: 22435804]
14. Kania E, Roest G, Vervliet T, Parys JB, Bultynck G. IP3 Receptor-Mediated Calcium Signaling and Its Role in Autophagy in Cancer. Front Oncol. 2017; 7:140. [PubMed: 28725634]
15. Ando H, Kawaai K, Bonneau B, Mikoshiba K. Remodeling of Ca2+signaling in cancer: Regulation of inositol 1,4,5-trisphosphate receptors through oncogenes and tumor suppressors. Advances in Biological Regulation. 2017; doi: 10.1016/j.jbior.2017.12.001
16. Berridge MJ. The Inositol Trisphosphate/Calcium Signaling Pathway in Health and Disease. Physiol Rev. 2016; 96:1261–1296. [PubMed: 27512009]
17. Egorova PA, Bezprozvanny IB. Inositol 1,4,5-trisphosphate receptors and neurodegenerative disorders. FEBS J. 2017; doi: 10.1111/febs.14366
18. Bezprozvanny I, et al. Bell-shaped calcium-response curves of lns(l,4,5)P3- and calcium-gated channels from endoplasmic reticulum of cerebellum. Nature. 1991; 351:751–754. [PubMed: 1648178]
19. Mikoshiba K. Role of IP3 receptor signaling in cell functions and diseases. Adv Biol Regul. 2015; 57:217–227. [PubMed: 25497594]
20. Gerasimenko OV, Gerasimenko JV, Belan PV, Petersen OH. Inositol trisphosphate and cyclic ADP-ribose-mediated release of Ca2+from single isolated pancreatic zymogen granules. Cell. 1996; 84:473–480. [PubMed: 8608601]
21. Iino M. Biphasic Ca2+ dependence of inositol 1,4,5-trisphosphate-induced Ca release in smooth muscle cells of the guinea pig taenia caeci. J Gen Physiol. 1990; 95:1103–22. [PubMed: 2373998]
22. Stehno-Bittel L, Lückhoff A, Clapham DE. Calcium release from the nucleus by InsP3 receptor channels. Neuron. 1995; 14:163–167. [PubMed: 7530018]
23. Bootman MD, Berridge MJ, Lipp P. Cooking with calcium: The recipes for composing global signals from elementary events. Cell. 1997; 91:367–373. [PubMed: 9363945]
24. Marchant JS, Parker I. Role of elementary Ca2+ puffs in generating repetitive Ca2+ oscillations. EMBO J. 2001; 20:65–76. [PubMed: 11226156]
25. Parker I, Choi J, Yao Y. Elementary events of InsP3-induced Ca2+liberation in Xenopus oocytes: Hot spots, puffs and blips. Cell Calcium. 1996; 20:105–121. [PubMed: 8889202]
26. Hajnóczky G, Thomas AP. Minimal requirements for calcium oscillations driven by the IP3 receptor. EMBO J. 1997; 16:3533–3543. [PubMed: 9218795]
27. Marshall IC, Taylor CW. Two calcium-binding sites mediate the interconversion of liver inositol 1,4,5-trisphosphate receptors between three conformational states. Biochem J. 1994; 301(Pt 2): 591–598. [PubMed: 8043006]

28. Sienaert I, et al. Molecular and functional evidence for multiple Ca2+-binding domains in the type 1 inositol 1,4,5-trisphosphate receptor. J Biol Chem. 1997; 272:25899–906. [PubMed: 9325322]
29. Striggow F, Ehrlich BE. The inositol 1,4,5-trisphosphate receptor of cerebellum. Mn2+ permeability and regulation by cytosolic Mn2+ J Gen Physiol. 1996; 108:115–124. [PubMed: 8854341]
30. Hamada K, Terauchi A, Mikoshiba K. Three-dimensional Rearrangements within Inositol 1,4,5-Trisphosphate Receptor by Calcium. J Biol Chem. 2003; 278:52881–52889. [PubMed: 14593123]
31. Shinohara T, et al. Mechanistic basis of bell-shaped dependence of inositol 1,4,5-trisphosphate receptor gating on cytosolic calcium. Proc Natl Acad Sci U S A. 2011; 108:15486–15491. [PubMed: 21876165]
32. Mak DOD, McBride S, Foskett JK. Inositol 1,4,5-tris-phosphate activation of inositol tris-phosphate receptor Ca2+ channel by ligand tuning of Ca2+ inhibition. Proc Natl Acad Sci. 1998; 95:15821–15825. [PubMed: 9861054]
33. Maranto AR. Primary structure, ligand binding, and localization of the human type 3 inositol 1,4,5-trisphosphate receptor expressed in intestinal epithelium. J Biol Chem. 1994; 269:1222–1230. [PubMed: 8288584]
34. Bosanac I, et al. Structure of the inositol 1,4,5-trisphosphate receptor binding core in complex with its ligand. Nature. 2002; 420:696–700. [PubMed: 12442173]
35. Bosanac I, et al. Crystal structure of the ligand binding suppressor domain of type 1 inositol 1,4,5-trisphosphate receptor. Mol Cell. 2005; 17:193–203. [PubMed: 15664189]
36. Lin CC, Baek K, Lu Z. Apo and InsP3-bound crystal structures of the ligand-binding domain of an InsP3 receptor. Nat Struct Mol Biol. 2011; 18:1172–1174. [PubMed: 21892169]
37. Seo MD, et al. Structural and functional conservation of key domains in InsP3 and ryanodine receptors. Nature. 2012; 483:108–112. [PubMed: 22286060]
38. Fan G, et al. Gating machinery of InsP3R channels revealed by electron cryomicroscopy. Nature. 2015; 527:336–341. [PubMed: 26458101]
39. Scheres SHW. Processing of Structurally Heterogeneous Cryo-EM Data in RELION. Methods in Enzymology. 2016; 579:125–157. [PubMed: 27572726]
40. des Georges A, et al. Structural Basis for Gating and Activation of RyR1. Cell. 2016; 167:145–157.e17. [PubMed: 27662087]
41. Prole DL, Taylor CW. Inositol 1,4,5-trisphosphate receptors and their protein partners as signalling hubs. Journal of Physiology. 2016; 594:2849–2866. [PubMed: 26830355]
42. Boehning D, Joseph SK. Direct association of ligand-binding and pore domains in homo- and heterotetrameric inositol 1,4,5-trisphosphate receptors. EMBO J. 2000; 19:5450–5459. [PubMed: 11032812]
43. Chan J, et al. Structural Studies of Inositol 1,4,5-Trisphosphate Receptor. J Biol Chem. 2010; 285:36092–36099. [PubMed: 20843799]
44. Uchida K, Miyauchi H, Furuichi T, Michikawa T, Mikoshiba K. Critical regions for activation gating of the inositol 1,4,5-trisphosphate receptor. J Biol Chem. 2003; 278:16551–16560. [PubMed: 12621039]
45. Yamazaki H, Chan J, Ikura M, Michikawa T, Mikoshiba K. Tyr-167/Trp-168 in type 1/3 inositol 1,4,5-trisphosphate receptor mediates functional coupling between ligand binding and channel opening. J Biol Chem. 2010; 285:36081–36091. [PubMed: 20813840]
46. McGoldrick LL, et al. Opening of the human epithelial calcium channel TRPV6. Nature. 2018; 553:233–237. [PubMed: 29258289]
47. Ionescu L, et al. Mode Switching Is the Major Mechanism of Ligand Regulation of InsP 3 Receptor Calcium Release Channels. J Gen Physiol. 2007; 130:631–645. [PubMed: 17998395]
48. Goehring A, et al. Screening and large-scale expression of membrane proteins in mammalian cells for structural studies. Nat Protoc. 2014; 9:2574–85. [PubMed: 25299155]
49. Whicher JR, MacKinnon R. Structure of the voltage-gated K+channel Eag1 reveals an alternative voltage sensing mechanism. Science (80-). 2016; 353:664–669.
50. Kirchhofer A, et al. Modulation of protein properties in living cells using nanobodies. Nat Struct Mol Biol. 2010; 17:133–139. [PubMed: 20010839]

51. Mastronarde DN. Automated electron microscope tomography using robust prediction of specimen movements. J Struct Biol. 2005; 152:36–51. [PubMed: 16182563]
52. Suloway C, et al. Automated molecular microscopy: The new Leginon system. J Struct Biol. 2005; 151:41–60. [PubMed: 15890530]
53. Zheng SQ, et al. MotionCor2: anisotropic correction of beam-induced motion for improved cryo-electron microscopy. Nat Methods. 2017; 14:331–332. [PubMed: 28250466]
54. Rohou A, Grigorieff N. CTFFIND4: Fast and accurate defocus estimation from electron micrographs. J Struct Biol. 2015; 192:216–221. [PubMed: 26278980]
55. Punjani A, Rubinstein JL, Fleet DJ, Brubaker M. A cryoSPARC: algorithms for rapid unsupervised cryo-EM structure determination. Nat Methods. 2017; 14:290–296. [PubMed: 28165473]
56. Grigorieff N, Grant T, Rohou A. cisTEM: User-friendly software for single-particle image processing. 2018; :257618. bioRxiv. doi: 10.1101/257618
57. Rosenthal PB, Henderson R. Optimal determination of particle orientation, absolute hand, and contrast loss in single-particle electron cryomicroscopy. J Mol Biol. 2003; 333:721–745. [PubMed: 14568533]
58. Pettersen EF, et al. UCSF Chimera - A visualization system for exploratory research and analysis. J Comput Chem. 2004; 25:1605–1612. [PubMed: 15264254]
59. Emsley P, Cowtan K. IUCr. Coot: model-building tools for molecular graphics. Acta Crystallogr Sect D Biol Crystallogr. 2004; 60:2126–2132. [PubMed: 15572765]
60. Drozdetskiy A, Cole C, Procter J, Barton GJ. JPred4: A protein secondary structure prediction server. Nucleic Acids Res. 2015; 43:W389–W394. [PubMed: 25883141]
61. Wang RYR, et al. Automated structure refinement of macromolecular assemblies from cryo-EM maps using Rosetta. Elife. 2016; 5
62. Adams PD, et al. PHENIX: A comprehensive Python-based system for macromolecular structure solution. Acta Crystallogr Sect D Biol Crystallogr. 2010; 66:213–221. [PubMed: 20124702]
63. Morin A, et al. Collaboration gets the most out of software. Elife. 2013; 2013:e01456.
64. Kucukelbir A, Sigworth FJ, Tagare HD. Quantifying the local resolution of cryo-EM density maps. Nat Methods. 2014; 11:63–65. [PubMed: 24213166]

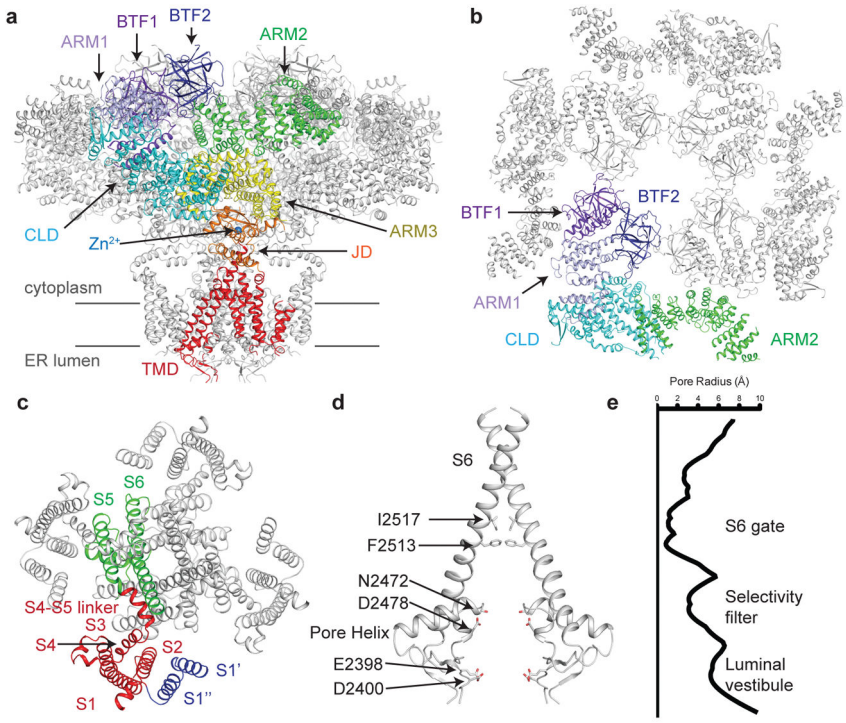

Figure 1. Structure of human type 3 IP_3R in a ligand-free state

a, Structure of hIP_3R3 viewed in the plane of the membrane with the cytoplasmic domain at the top. A single subunit is colored according to domain with BTF1 in purple, BTF2 in blue, ARM1 in violet, the CLD in cyan, ARM2 in green, ARM3 in yellow, the JD in orange and the TMD in red. Gray lines represent the approximate position of the membrane. **b,** Structure of the cytoplasmic domain viewed from the cytoplasm. A single subunit is colored according to domain. ARM3 is removed for clarity. **c,** Structure of the transmembrane domain viewed from the cytoplasm. S1–S4 helices are colored red, S1′ and S1″ blue and S5, S6 and pore helix green. **d–e,** Structure of the ion conduction pathway viewed in the plane of the membrane and plot of pore radius. Residues comprising the luminal vestibule, the selectivity filter and S6 gate are highlighted. Front and rear subunits are removed for clarity.

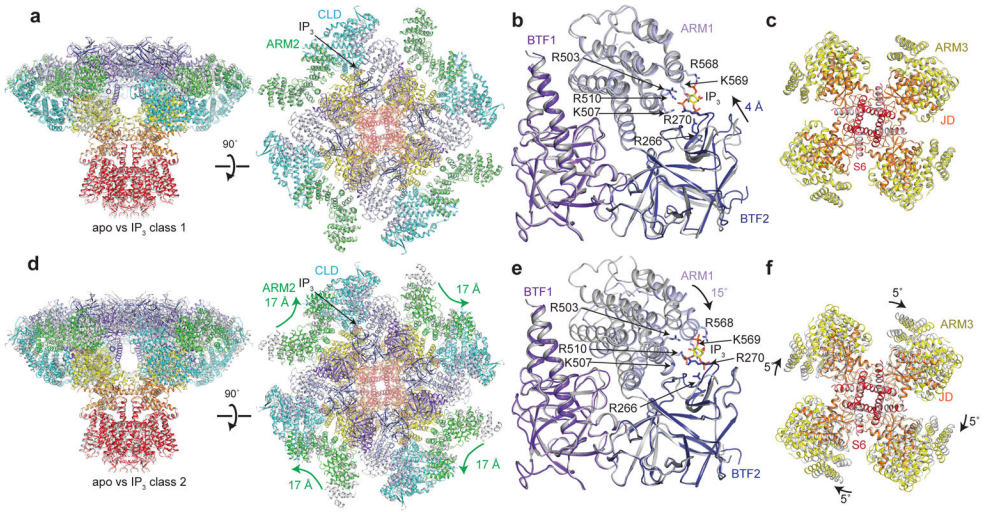

Figure 2. IP_3 binding site in two IP_3-bound conformations

a, d, Superposition of (**a**) IP_3 class 1 (colored by domain) and apo (grey) or (**d**) IP_3 class 2 (colored by domain) and apo (grey) viewed from in the plane of the membrane (left) and the cytoplasm (right). **b, e,** Superposition of IP_3-binding domain of (**b**) IP_3 class 1 (colored by domain) and apo (grey) or (**e**) IP_3 class 2 (colored by domain) and apo (grey) aligned by BTF1 and BTF2. IP_3 and the side chains of IP_3-coordinating residues are shown as sticks. **c, f,** Superposition of ARM3, the JD and S6 of (**c**) IP_3 class 1 (colored by domain) and apo (grey) or (**f**) IP_3 class 2 (colored by domain) and apo (grey) aligned by the TMD and viewed from the lumen.

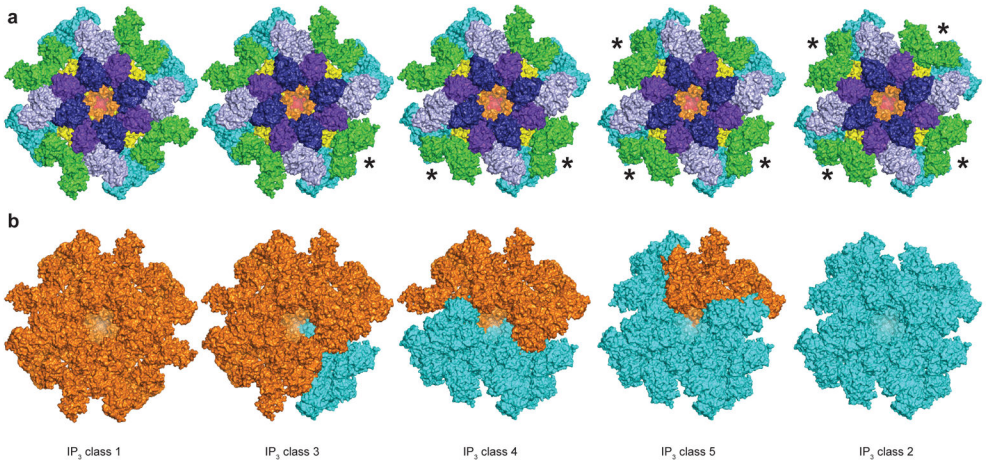

Figure 3. Ensemble of IP_3-bound conformations

a, Structures of IP_3 class 1, IP_3 class 32, IP_3 class 4, IP_3 class 5 and IP_3 class 2 colored by domain. The ARM2 domain of subunits marked with an * adopt a class 2-like conformation. **b,** Structures of IP_3 class 1, IP_3 class 3, IP_3 class 4, IP_3 class 5 and IP_3 class 2. Domains adopting class 1-like domains are colored orange and domains adopting class 2-like conformations are colored cyan.

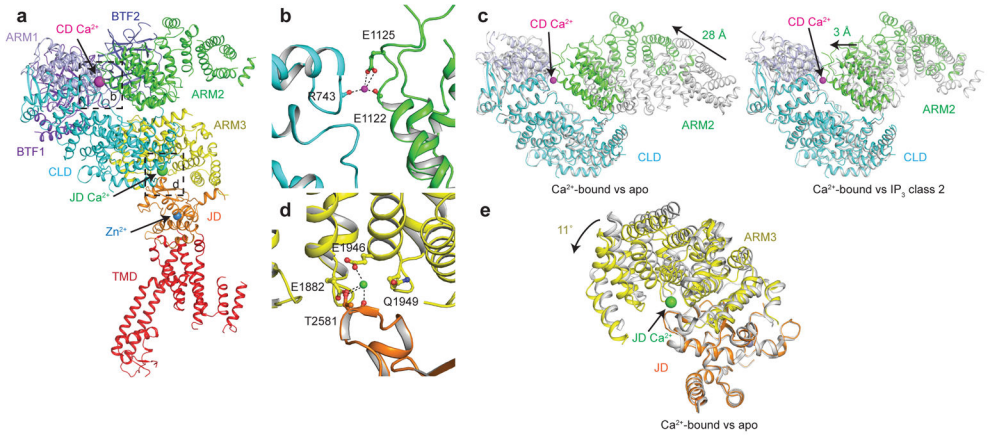

Figure 4. Ca^{2+} binding sites in Ca^{2+}-bound hIP_3R3

a, Monomeric structure of Ca^{2+}-bound hIP_3R3 colored by domain viewed in the plane of the membrane. Ca^{2+} and Zn^{2+} ions are shown as spheres. **b,** CD Ca^{2+}-binding site at the CLD-ARM2 interface. Residues coordinating the Ca^{2+} are shown as sticks and the CD Ca^{2+} ion is shown as a magenta sphere. **c,** Superposition of the CLD and ARM2 of Ca^{2+}-bound (colored by domain) and apo (grey, left) or Ca^{2+}-bound (colored by domain) and IP_3 class 2 (grey, right) aligned by the CLD. **d,** JD Ca^{2+}-binding site at the ARM3-JD interface. Residues coordinating the Ca^{2+} are shown as sticks and the Ca^{2+} ion is shown as a green sphere. **e,** Superposition of ARM3 and the JD of Ca^{2+}-bound (colored by domain) and apo (grey) aligned by the JD.

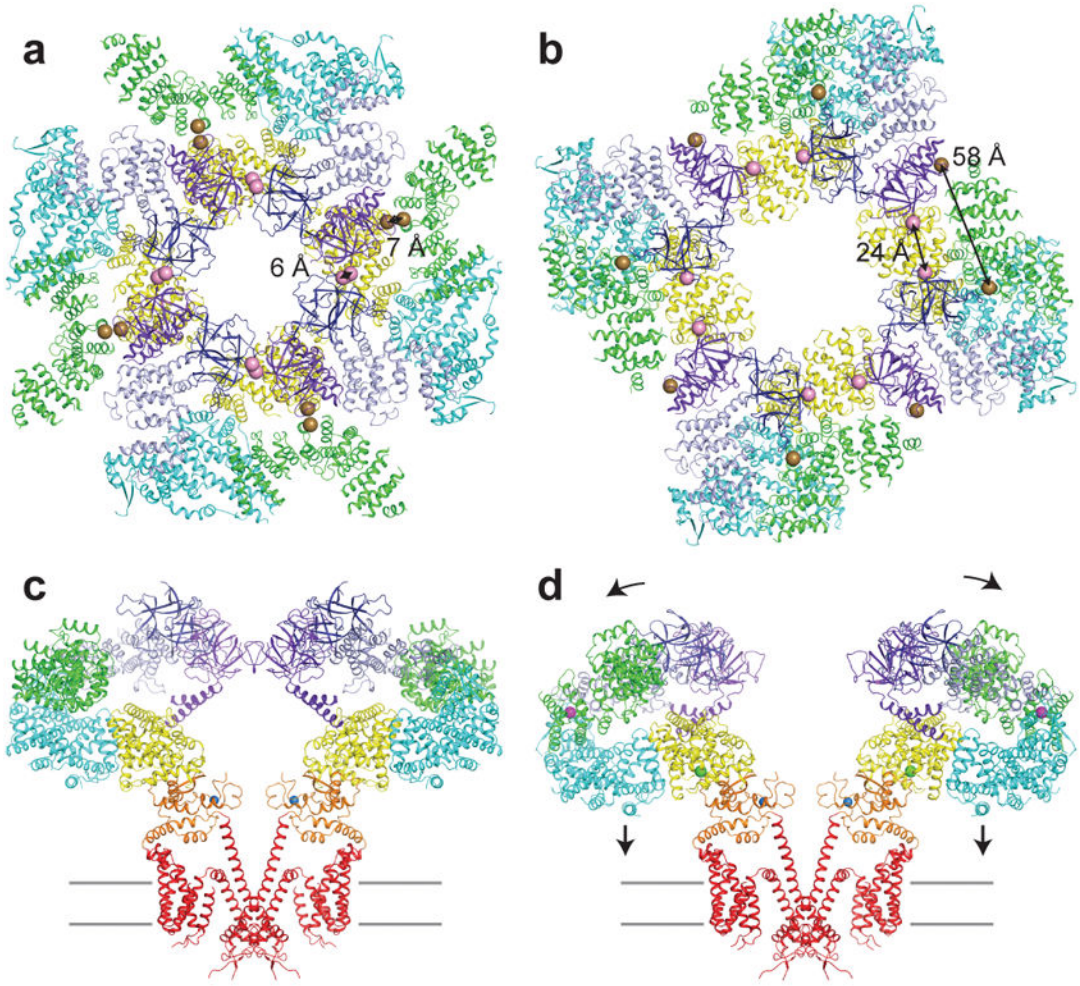

Figure 5. Ca^{2+} binding disrupts CD intra- and inter-subunit interactions

a–b, Cytoplasmic domain of (**a**) apo and (**b**) Ca^{2+}-bound colored by domain, viewed from the cytoplasm. Spheres represent the Cα position of Trp168 of BTF1 and Lys426 of BTF2 (pink) and Pro140 of BTF1 and Ala1291 of ARM2 (brown). **c–d,** Structure of (**c**) apo and (**d**) Ca^{2+}-bound colored by domain, viewed in the plane of the membrane. Front and rear subunits are removed for clarity. Ca^{2+} and Zn^{2+} ions are shown as spheres. Grey lines represent the approximate position of the membrane.

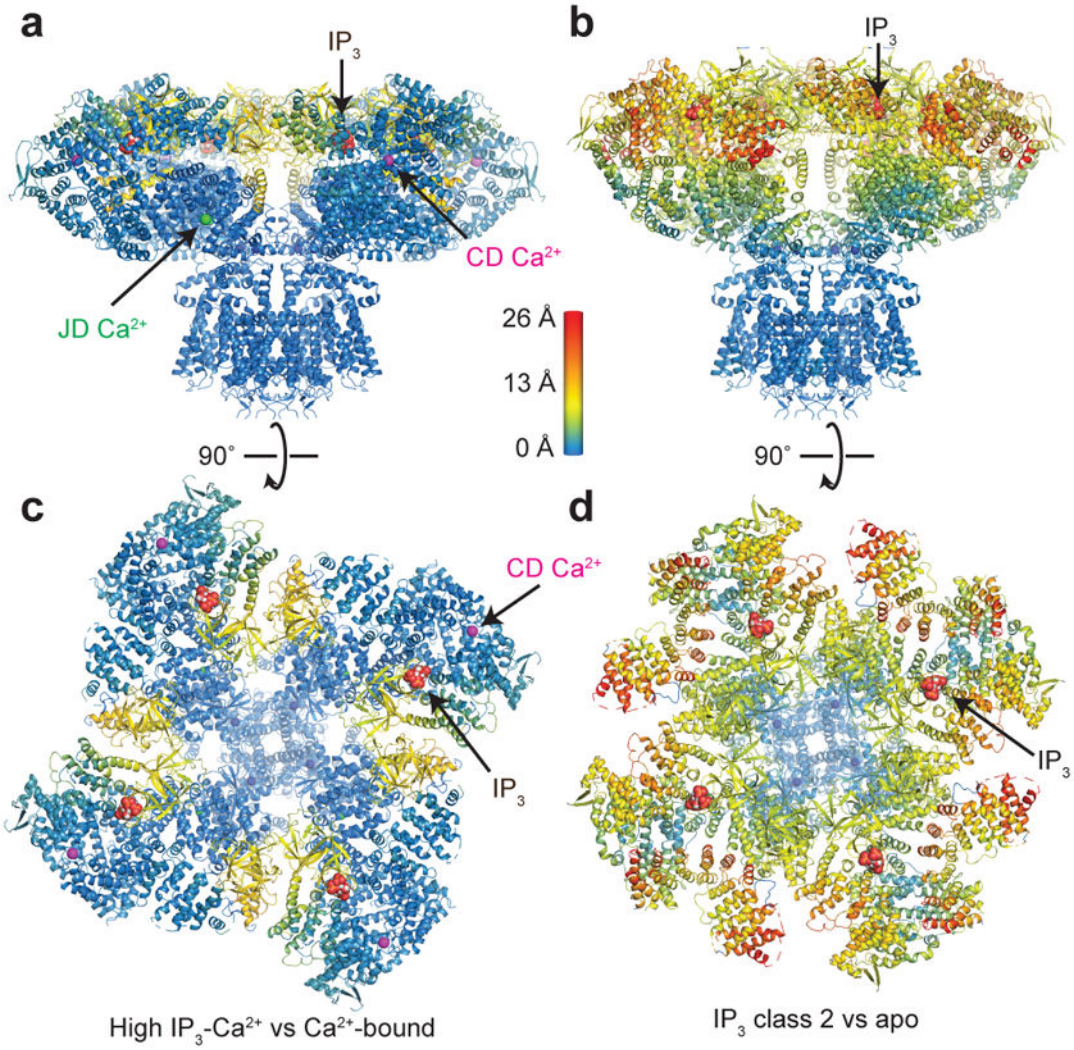

Figure 6. IP_3-induced conformational changes

a, High IP_3-Ca^{2+} structure colored by distance of Cα deviation from the Ca^{2+}-bound structure viewed in the plane of the membrane. **b,** IP_3 class 2 colored by distance of Cα deviation from the apo structure viewed in the plane of the membrane. **c,** Cytoplasmic domain of high IP_3-Ca^{2+} structure colored by distance of Cα deviation from the Ca^{2+}-bound structure viewed from the cytoplasm. **d,** Cytoplasmic domain of IP_3 class 2 colored by distance of Cα deviation from the apo structure viewed from the cytoplasm. IP_3 and Ca^{2+} ions are shown as spheres.

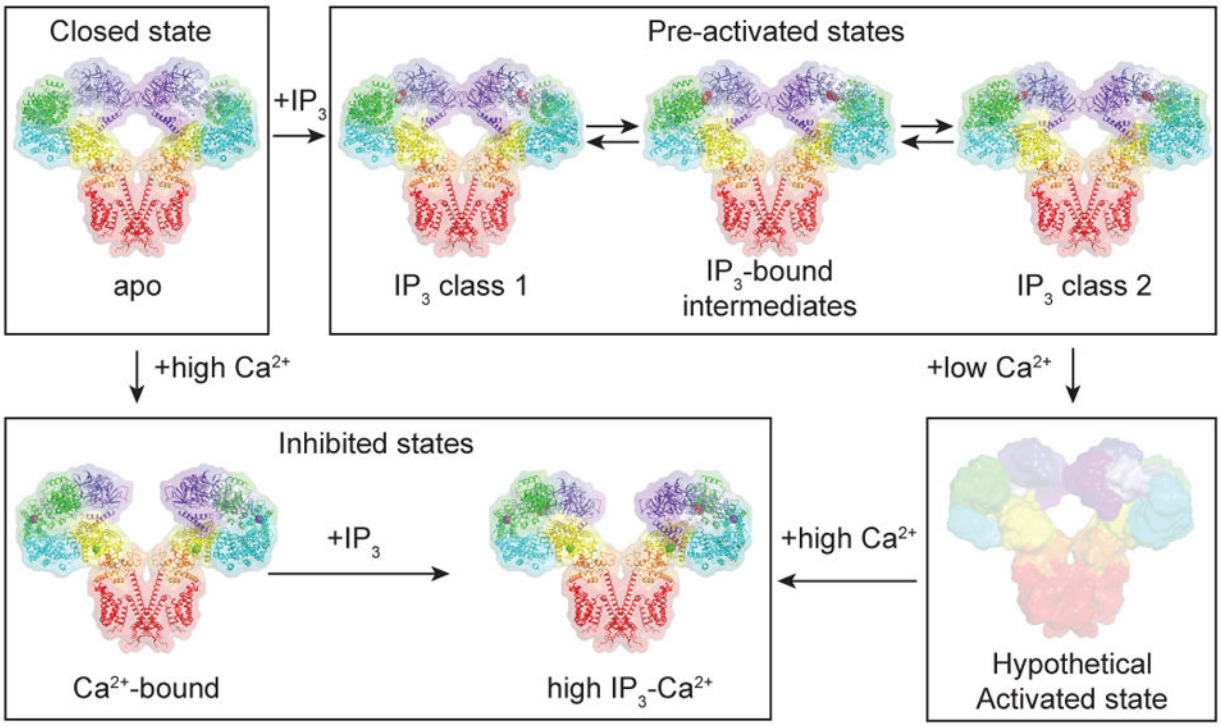

Figure 7. Model for IP_3R regulation by IP_3 and Ca^{2+}

In the absence of Ca^{2+} and IP_3, IP_3R adopts a closed state. In the presence of IP_3, IP_3R adopts one of an ensemble of pre-activated states that are in equilibrium. In the presence of high Ca^{2+}, the BTF ring is dissociated and the channel adopts an inhibited state. In the presence of high Ca^{2+} and IP_3, the BTF ring is dissociated and the channel adopts an inhibited state. In the presence of low Ca^{2+} and IP_3, the channel adopts a hypothetical activated state in which the S6 gate is opened.

Table 1

Cryo-EM data collection, refinement and validation statistics.

	hIP$_3$R3 apo (EMD-7978) (PDB 6DQJ)	**hIP$_3$R3 IP$_3$ class 1 (EMB-7981) (PDB 6DQN)**	**hIP$_3$R3 IP$_3$ class 2 (EB-7984) (PDB 6DQV)**	**hIP$_3$R3 IP$_3$ class 3 (EMB-7983) (PDB 6DQS)**	**hIP$_3$R3 IP$_3$ class 4 (EMB-7986) (PDB 6DQZ)**	**hIP$_3$R3 IP$_3$ class 5 (EMB-7987) (PDB 6DR0)**	**hIP$_3$R3 Ca^{2+}-bound (EMB-7988) (PDB 6DR2)**	**hIP$_3$R3 Low IP$_3$-Ca^{2+} (EMB-7991) (PDB 6DRA)**	**hIP$_3$R3 High IP$_3$-Ca^{2+} (EMB-7994) (PDB 6DRC)**
Data collection and processing									
Magnification	105,000x	22,500x	22,500x	22,500x	22,500x	22,500x	22,500x	22,500x	22,500x
Voltage (kV)	300kV	300kV	300kV	300kV	300kV	300kV	300kV	300kV	300kV
Electron exposure (e–/Å^2)	60	61	61	61	61	61	61	61	61
Defocus range (μm)	−1.0 – 2.5	−1.0 – 2.5	−1.0 – 2.5	−1.0 – 2.5	−1.0 – 2.5	−1.0 – 2.5	−1.0 – 2.5	−1.0 – 2.5	−1.0 – 2.5
Pixel size (Å)	1.096	1.088	1.088	1.088	1.088	1.088	1.088	1.088	1.088
Symmetry imposed	C4	C4	C4	C1	C1	C1	C4	C4	C4
Initial particle images (no.)	52,767	302,966	302,966	302,966	302,966	302,966	49,060	74,277	170,308
Final particle images (no.)	26,325	38,777	40,531	37,910	9,535	27,334	33,807	49,087	131,437
Map resolution (Å)	3.49	3.33	3.82	4.12	6.01	4.47	4.33	3.96	3.92
FSC threshold	0.143	0.143	0.143	0.143	0.143	0.143	0.143	0.143	0.143
Map resolution range (Å)	300-3.49	300-3.33	300-3.82	300-4.12	300-6.01	300-4.47	300-4.33	300-3.96	300-3.92
Refinement									
Initial model used (PDB code)	3UJ4								
Model resolution (Å)	3.80/3.35	3.88/3.36	4.53/3.93	4.83/3.90	7.63/6.33	7.06/4.23	7.44/4.34	4.49/3.91	4.43/3.92
FSC threshold	0.50/0.143	0.50/0.143	0.50/0.143	0.50/0.143	0.50/0.143	0.50/0.143	0.50/0.143	0.50/0.143	0.50/0.143
Model resolution range (Å)	300-3.5	300-3.3	300-3.8	300-4.1	300-6.0	300-4.5	300-4.3	300-4.0	300-4.0
Map sharpening *B* factor (Å^2)	−90	−90	−90	−90	−90	−90	−90	−90	−90
Model composition									
Non-hydrogen	69,220	69,412	70,144	69,600	69,828	69,986	69,3572	69,572	69,508
Protein residues	8,744	8,744	8,752	8,750	8,748	8,750	8,764	8,764	8,744
Ligands	4	8	8	8	8	8	12	12	16
Mean *B* factors (Å^2)									
Protein	95.1	116.1	169.0	193.5	376.7	217.0	239.9	240.0	217.9
Ligand	53.5	96.95	133.0	177.4	362.0	182.9	174.7	163.6	263.3

	hIP$_3$R3 apo (EMD-7978) (PDB 6DQJ)	**hIP$_3$R3 IP$_3$ class 1 (EMB-7981) (PDB 6DQN)**	**hIP$_3$R3 IP$_3$ class 2 (EB-7984) (PDB 6DQV)**	**hIP$_3$R3 IP$_3$ class 3 (EMB-7983) (PDB 6DQS)**	**hIP$_3$R3 IP$_3$ class 4 (EMB-7986) (PDB 6DQZ)**	**hIP$_3$R3 IP$_3$ class 5 (EMB-7987) (PDB 6DR0)**	**hIP$_3$R3 Ca^{2+}-bound (EMB-7988) (PDB 6DR2)**	**hIP$_3$R3 Low IP$_3$-Ca^{2+} (EMB-7991) (PDB 6DRA)**	**hIP$_3$R3 High IP$_3$-Ca^{2+} (EMB-7994) (PDB 6DRC)**
R.m.s. deviations									
Bond lengths (Å)	0.007	0.003	0.005	0.003	0.003	0.003	0.004	0.003	0.004
Bond angles (°)	0.688	0.490	0.648	0.520	0.536	0.538	0.660	0.517	0.623
Validation									
MolProbity score	1.53	1.21	1.36	1.28	1.22	1.26	1.26	1.24	1.33
Clashscore	2.16	2.09	2.22	2.41	2.43	2.37	2.07	2.96	2.14
Poor rotamers (%)	1.97	1.06	0.00	0.00	0.00	0.00	0.00	0.42	0.00
Ramachandran plot									
Favored (%)	95.52	96.70	94.74	96.14	96.8	96.33	95.91	97.12	95.04
Allowed (%)	4.48	3.30	5.26	3.86	3.20	3.67	4.09	2.88	4.96
Disallowed (%)	0.00	0.00	0.00	0.00	0.00	0.00	0.00	0.00	0.00